A Comprehensive Spatial-Temporal Channel Propagation Model for the Ultrawideband Spectrum 2–8 GHz

Camillo Gentile, Sofía Martínez López, and Alfred Kik

***Abstract*—Despite the potential for high-speed communications, stringent regulatory mandates on ultrawideband (UWB) emission have hindered its commercial success. By combining resolvable UWB multipath from different directions, multiple-input multiple-output (MIMO) technology can drastically improve link robustness or range. In fact, a plethora of algorithms and coding schemes already exist for UWB-MIMO systems, however these papers use simplistic channel models in simulation and testing. While the temporal characteristics of the UWB propagation channel have been well documented, surprisingly there currently exists but a handful of spatial-temporal models to our knowledge, and only two for bandwidths in excess of 500 MHz. This paper proposes a comprehensive spatial-temporal channel propagation model for the frequency spectrum 2–8 GHz, featuring a host of novel parameters. In order to extract the parameters, we conduct an extensive measurement campaign using a vector network analyzer coupled to a virtual circular antenna array. The campaign includes 160 experiments up to a non line-of-sight range of 35 meters in four buildings with construction material varying from sheetrock to steel.**

***Index Terms*—Multiple-input multiple-output (MIMO), uniform circular array.**

I. Introduction

ULTRAWIDEBAND (UWB) technology is characterized by a bandwidth greater than 500 MHz or exceeding 20% of the center frequency of radiation [1]. Despite the potential for high-speed communications, the FCC mask of −41.3 dBm/MHz EIRP in the spectrum 3.1–10.6 GHz translates to a maximum transmission power of −2.6 dBm. This limits applications to moderate data rates or short range. Multiple-input multiple-output (MIMO) communication systems exploit spatial diversity by combining multipath arrivals from different directions to drastically improve link robustness or range [2]. Ultrawideband lends to MIMO by enabling multipath resolution through its fine time pulses and the fact that most UWB applications are geared towards indoor environments rich in scattering provides an ideal reception scenario for MIMO implementation; in addition, the GHz center frequency relaxes the mutual-coupling requirements on the spacing between antenna array elements. For these reasons UWB and MIMO fit hand-in-hand, making the best possible use of radiated power to promote the commercial success of UWB communication systems.

In fact, a plethora of algorithms and coding schemes already exist for UWB-MIMO systems, exploiting not only spatial diversity, but time and frequency diversity as well [3]–[5]. Yet these papers use simplistic channel models in simulation and testing. While the temporal characteristics of the UWB channel have been well documented in [1], [6]–[14], surprisingly there currently exists but a handful of spatial-temporal channel models to our knowledge [15]–[21], and only two for UWB with bandwidths in excess of 500 MHz [22], [23]. Most concentrate on independently characterizing a few parameters of the channel, but none furnish a comprehensive model in multiple environments which allows total reconstruction of the spatial-temporal response, analogous to the pioneering work in the UWB temporal model of Molisch *et al.* [1]. In order to fill this void, we propose a detailed UWB spatial-temporal model. Specifically, the main contributions of this paper are:

- *a frequency-dependent pathgain model*: allows reconstructing the channel for any subband within $f = 2$–8 GHz, essential to test schemes using frequency diversity, and incorporates frequency-distance dependence previously modeled separately;
- *a spatial-temporal response model*: introduces the distinction between spatial clusters and temporal clusters, and incorporates spatial-temporal dependence previously modeled separately;
- *diverse construction materials*: to model typical building construction materials varying as sheetrock, plaster, cinder block, and steel rather than with building layout (i.e. office, residential typically have the same wall materials);
- *high dynamic range*: the high dynamic range of our system allows up to 35 meters in non line-of-sight (NLOS) range to capture the effect of interaction with up to 10 walls in the direct path between the transmitter and receiver.

The paper reads as follows: Section II describes the frequency and spatial diversity techniques used to measure the spatial-temporal propagation channel. The subsequent section explains the

Manuscript received October 23, 2008; revised October 13, 2009; accepted December 24, 2009. Date of publication March 29, 2010; date of current version June 03, 2010.

C. Gentile is with the Emerging and Wireless Networking Technologies Group, Advanced Network Technologies Division, National Institute of Standards and Technology, Gaithersburg, MD 20899 USA (e-mail: camillo.gentile@nist.gov).

S. M. López was with the National Institute of Standards and Technology, Emerging and Wireless Networking Technologies Group, Gaithersburg, MD 20899 USA. She is now with Orange-France Télécom Group, Portet-sur-Garonne, 31128, France.

A. Kik is with the Tokyo Institute of Technology, Tokyo 152-8550 Japan.

Color versions of one or more of the figures in this paper are available online at http://ieeexplore.ieee.org.

Digital Object Identifier 10.1109/TAP.2010.2046834

0018-926X/$26.00 © 2010 IEEE

design and specifications of our measurement system realized through a vector network analyzer coupled to a virtual circular antenna array, and outlines our suite of measurements. The main Section IV features our proposed stochastic model characterizing the channel with parameters reported individually for eight different environments; given the wealth of accumulated data furnished through our measurement campaign, we attempt to reconcile the sometimes contradictory findings amongst other models due to limited measurements. The last section summarizes our conclusions.

II. Measuring the Spatial-Temporal Response

A. Measuring the Temporal Response Through Frequency Diversity

The temporal response $h(t)$ of the indoor propagation channel is composed from an infinite number of multipath arrivals indexed through k

$$h(t) := \sum_{k=1}^{\infty} a_k e^{j\varphi_k} \delta(t - \tau_k) \tag{1}$$

where τ_k denotes the delay of the arrival in propagating the distance d between the transmitter and receiver, and the complex-amplitude $a_k e^{j\varphi_k}$ accounts for both attenuation and phase change due to reflection, diffraction, and other specular effects introduced by walls (and other objects) on its path.

The temporal response $h(t)$ has a frequency response

$$H(f) = \sum_{k=1}^{\infty} a_k e^{j\varphi_k} e^{-j2\pi f \tau_k} \tag{2}$$

suggesting that the channel can be characterized through *frequency diversity*: we sample $H(f) = Y(f)/X(f)$ at rate Δf by transmitting tones $X(f)$ across the channel and then measuring $Y(f)$ at the receiver. Characterizing the channel in the frequency domain offers two important advantages over transmitting a UWB pulse and recording the temporal response directly: 1) it enables extracting the frequency parameter α; 2) a subband with bandwidth B and center frequency f_c can be selected a posteriori in reconstructing the channel. The discrete frequency spectrum $X(f)$ transforms to a signal with period $1/\Delta f$ in the time domain [26], and so choosing $\Delta f = 1.25$ MHz allows for a maximum multipath spread of 800 ns which proves sufficient throughout all four buildings for the arrivals to subside within one period and avoid time aliasing.

B. Measuring the Spatial Response Through Spatial Diversity

Replacing the single antenna at the receiver with an antenna array introduces *spatial diversity* into the system. This enables measuring both the temporal and spatial properties of the UWB channel. We chose to implement the uniform circular array (UCA) over the uniform linear array (ULA) in light of the following two important advantages: 1) the azimuth of the UCA covers 360° in contrast to the 180° of the ULA; 2) the beam pattern of the UCA is uniform around the azimuth angle while that of the ULA broadens as the beam is steered from the boresight.

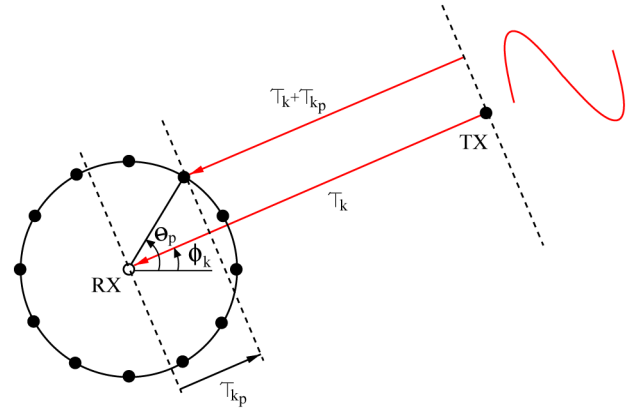

Fig. 1. The uniform circular array antenna.

Consider the diagram in Fig. 1 of the uniform circular array. The P elements of the UCA are arranged uniformly around its perimeter of radius r, each at angle $\theta_p = (2\pi i/P), p = 1 \ldots P$. The radius determines the half-power beamwidth corresponding to $29.2°(c/r \cdot f_c)$ [27]. Let $H(f)$ be the frequency response of the channel between the transmitter and reference center of the receiver array. Arrival k approaching from angle ϕ_k hits element p with a delay $\tau_{k_p} = -(r/c)\cos(\phi_k + \theta_p)$ with respect to the center [28], hence the element frequency response $H_p(f)$ is a phase-shifted version of $H(f)$ by the steering vector, or

$$H_p(f) = H(f)e^{-j2\pi f \tau_{k_p}} = H(f)e^{j2\pi f \frac{r}{c}\cos(\phi_k + \theta_p)}. \tag{3}$$

The array frequency response $H(f, \theta)$ is generated through beamforming by shifting the phase of each element frequency response $H_p(f)$ back into alignment at the [28]

$$H(f, \theta) = \frac{1}{P} \sum_{p=1}^{P} H_p(f) e^{-j2\pi f \frac{r}{c}\cos(\theta + \theta_p)}. \tag{4}$$

The spatial-temporal response $h(t, \theta)$ can then be recovered through the inverse discrete Fourier transform of its array frequency response by synthesizing all the frequencies in the subband

$$h(t, \theta) = \frac{1}{\frac{B}{\Delta f}} \sum_{l=1}^{\frac{B}{\Delta f}} H(f, \theta) e^{j2\pi f t} \tag{5}$$

where $f = f_c - (B/2) + l \cdot \Delta f$.

III. The Measurement System and Campaign

A. The Measurement System

Fig. 2 displays the block diagram (a) and a photograph (b) of our measurement system. The transmitter antenna is mounted on a tripod while the UCA with $r = 24$ cm was realized virtually by mounting the receiver antenna on a positioning table. We sweep the $P = 97$ elements of the array by automatically repositioning the receiver at successive angles θ_p around its perimeter. At each element p, a vector network analyzer (VNA) in turn sweeps the discrete frequencies in the 2–8 GHz band. A total channel measurement, comprising the element sweep and the frequency

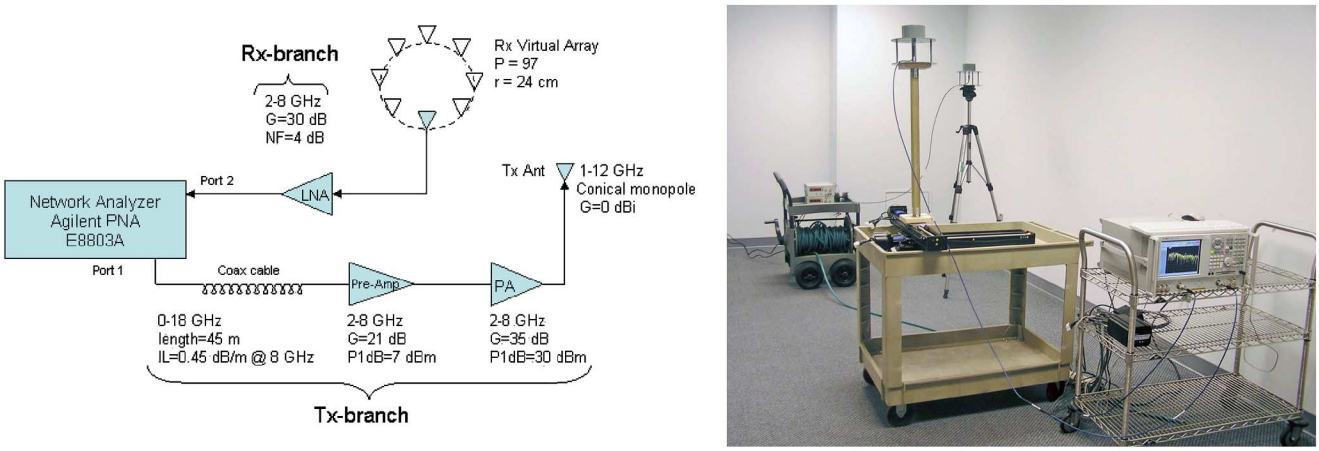

(a) (b)

Fig. 2. The measurement system using a vector network analyzer and a virtual circular antenna array. (a) Block diagram; (b) photograph.

sweep at each element, takes about 24 minutes. To eliminate disturbance due to the activity of personnel throughout the buildings and guarantee a static channel during the complete sweep, the measurements were conducted after working hours.

During the frequency sweep, the VNA emits a series of tones with frequency f at Port 1 and measures the relative amplitude and phase $S^{21}(f)$ with respect to Port 2, providing automatic phase synchronization between the two ports. The long cable enables variable placement of the transmitter and receiver antennas from each other throughout the test area. The height of the two identical conical monopole antennas was set to 1.7 m (average human height). The preamplifier and power amplifier on the transmit branch boost the signal such that it radiates at approximately 30 dBm from the antenna. After it passes through the channel, the low-noise amplifier (LNA) on the receiver branch boosts the signal above the noise floor of Port 2 before feeding it back.

The $S_p^{21}(f)$-parameter of the network in Fig. 2 can be expressed as follows:

$$\begin{aligned} S_p^{21}(f) &= H_{Tx}^{bra}(f)\cdot H_{Rx}^{bra}(f)\cdot\sum_{k=1}^{\infty} H_{Tx}^{ant}(f)_k\cdot H_p(f)_k\cdot H_{Rx}^{ant}(f)_k \\ &= H_{Tx}^{bra}(f)\cdot H_{Rx}^{bra}(f)\cdot H_{Tx}^{ant}(f)\cdot H_{Rx}^{ant}(f)\cdot\sum_{k=1}^{\infty} H_p(f)_k \\ &= H^{bra}(f)\cdot H^{ant}(f)\cdot H_p(f) \end{aligned} \tag{6}$$

where the antenna transfer functions $H_{Tx}^{ant}(f)_k$ and $H_{Rx}^{ant}(f)_k$ are indexed by k to account for the dependence of the antenna gains on the azimuth and elevation of the departure and arrival paths. These terms are approximated to angle independent terms since the interior elevation angle of the conical radiation pattern of the antennas is less than 40° and close to uniform in that small spread, and also because we employed a technique described in [29] which spatially averages the response by rotating the antennas with respect to each other every ten degrees. The branch response $H^{bra} = H_{Tx}^{bra}\cdot H_{Rx}^{bra}$ was measured in a closed-circuit fashion through a full two-port calibration step. Finally, in order to characterize the antenna response $H^{ant} = H_{Tx}^{ant}\cdot H_{Rx}^{ant}$, we separated the antennas by a distance of 1.5 m to avoid near-field operation. The antenna calibration was carried out on a flat open field with dimensions exceeding 100 m × 100 m to minimize ambient multipath to a single ground bounce which we subsequently removed by placing electromagnetic absorbers on the ground at their midpoint. Both antennas were set to a height of 1.7 m (average human height). Note in particular the following implementation considerations:

- to account for the frequency-dependent loss in the long cable when operating across such a large bandwidth, we ramped up the power at Port 1 with increasing frequency to equalize the radiated power from the transmitter across the whole band;
- we removed the LNA from the network in experiments with range below 10 m to protect it from overload and also avert its operation in the non-linear region;
- to extend the dynamic range of our system, we exploited the configurable test set option of the VNA to reverse the signal path in the coupler of Port 2 and bypass the 12 dB loss associated with the coupler arm. The dynamic range of the propagation channel corresponds to 140 dB as computed through [30] for an IF bandwidth of 1 kHz and a SNR of 15 dB at the receiver.

B. The Measurement Campaign

The measurement campaign was conducted in four separate buildings on the NIST campus in Gaitherburg, Maryland, each constructed from a dominant wall material varying from sheet rock to steel. Table I summarizes the 40 experiments in each building (10 LOS and 30 NLOS), including as an element the maximum number of walls separating the transmitter and receiver. As an example, consider the floor plan of *NIST North* in Fig. 3: the experiments were drawn from two sets of 22 transmitter locations and 4 receiver locations (marked by the empty and solid circles respectively) to the end of achieving a uniform distribution in range in both LoS and NLoS conditions. The solid line identifies the experiment with the longest range traversing 9 walls between the transmitter and receiver. The ground-truth distance d and ground-truth angle ϕ_0 between the transmitter and receiver were calculated in each experiment by pinpointing their coordinates on site with a laser tape, and subsequently finding these values using a computer-aided design (CAD) model of each building floor plan.

TABLE I
EXPERIMENTS CONDUCTED IN MEASUREMENT CAMPAIGN

building	wall material	LOS range (10)	NLOS range (30)
NIST North	sheet rock / aluminum studs	4.2-23.4 m	7.2-35.1 m max wall#: 9
Child Care	plaster / wooden studs	2.6-15.3 m	7.8-32.4 m max wall#: 8
Sound	cinder block	7.4-43.7 m	2.4-32.5 m max wall#: 10
Plant	steel	7.2-41.7 m	2.1-34.2 m max wall#: 10

Fig. 3. The building plan of *NIST North*.

IV. THE PROPOSED SPATIAL-TEMPORAL CHANNEL PROPAGATION MODEL

This section describes the proposed spatial-temporal channel propagation model. It is divided into two components: 1) the *reference spatial-temporal response* characterizes the shape of the two-dimensional multipath profile $h(t,\theta)$ and 2) the *frequency-dependent pathgain* scales its amplitude according to the distance between the transmitter and receiver and the frequency band of operation. The two corresponding subsections explain the extraction and modeling of the parameters of each component, following by a subsection that outlines in pseudocode how to implement the parameters to generate a stochastic channel response in the eight environments.

A. The Frequency-Dependent Pathgain Model

The frequency-dependent *excess* pathgain[1] is defined as

$$\begin{aligned} PG(f) &= |H(f)|^2 \\ &= \frac{1}{P}\sum_{p=1}^{P}|H_p(f)|^2 \end{aligned} \tag{7}$$

[1]There are alternative definitions to ours for the pathgain as summarized in [31].

and so can equivalently be computed for each experiment through the measured element frequency response in (3). In order to generate a model for the pathgain, consider decomposing the arrival amplitude in (2)

$$a_k = \tilde{a}_k \left(\frac{d}{d_0}\right)^{\frac{n}{2}} \left(\frac{f}{f_c}\right)^{\frac{\alpha}{2}} \tag{8}$$

as a product of the *reference* amplitude $\tilde{a}_k$ valid at reference point (d_0, f_c) and the *pathgain factor* representing the distance and frequency dependences of the amplitude. Incorporating the frequency parameter α into the model in addition to the conventional attenuation coefficient n [25] has been shown to improve channel reconstruction up to 40% for bandwidths in excess of 2 GHz [24]. Now by substituting (2) into (7) and expanding, the pathgain model can be written explicitly in terms of d to account for the distance of each experiment as

$$\begin{aligned} &(a)\quad PG(d,f) = \underbrace{PG(d_0,f_c)\left(\frac{d}{d_0}\right)^{-n}}_{PG(d,f_c)} \left(\frac{f}{f_c}\right)^{\alpha}; \\ &(b)\ PG(d_0,f_c) = \sum_{k=1}^{\infty}\tilde{a}_k^2. \end{aligned} \tag{9}$$

The reference pathgain $PG(d_0, f_c)$ for $d_0 = 1$ m and the attenuation coefficient n were extracted at the center frequency $f_c = 5$ GHz by fitting the model above to the data points of the experiments given with varying distance from (7). We actually found the breakpoint model [9] to represent the data much more accurately

$$PG(d,f_c) = \begin{cases} PG(d_0,f_c)\left(\frac{d}{d_0}\right)^{-n_0}\cdot 10^{\frac{s_d}{10}}, & d \le d_1 \\ PG(d_1,f_c)\left(\frac{d}{d_1}\right)^{-n_1}\cdot 10^{\frac{s_d}{10}}, & d > d_1 \end{cases} \tag{10}$$

augmented by the long-established parameter $s_d \sim \mathcal{N}(s_d; 0, \sigma_d)$ which quantifies the deviation between our model and the measured data and in that capacity represents the stochastic nature of the pathgain. Next the frequency parameter α in (9a) was fit to the remaining data points by allowing the frequency to vary. Based on the geometric theory of diffraction, in previous work [32] we noticed that wall interactions such as transmission, reflection, and diffraction increase α from the free space propagation value of zero. As the number of expected interactions increases with distance, a linear dependence of the frequency parameter on d can be observed and modeled as

$$\alpha(d) = \alpha_0 + \alpha_1 \cdot d \tag{11}$$

with positive slope α_1 through all environments.[2] Fig. 6(a) illustrates the frequency parameter versus the distance for the experiments in the *Child Care* in NLOS environment and Table II lists the parameters of the pathgain model for all eight environments.

[2]Only *Child Care* in LOS exhibited a small negative slope due to lack of data where the building structure limited the longest LOS distance to only 15.3 m.

TABLE II
THE PARAMETERS OF THE PROPOSED SPATIAL-TEMPORAL CHANNEL MODEL FOR THE EIGHT ENVIRONMENTS

environment		pathgain							N	delay				angle		amplitude					
	building	$PG(d_0,f_c)$ (dB)	n_0	n_1	d_1 (m)	σ_d (dB)	α_0	α_1 (m^{-1})	η	Υ	L (ns)	Λ (ns)	λ (ns)	υ (^{o}/ns)	σ (^{o})	Γ (ns)	γ_0 (ns)	γ_1	β_0 (^{o})	β_1 (^{o}/ns)	σ_s (dB)
NLOS	*NIST North*	-39.3	2.2	6.0	11	3.7	1.7	.015	2.0	0.01	6.2	25.2	0.82	0.13	32.1	22.6	47	.015	230	-1.4	2.8
	Child Care	-45.4	2.0	6.3	10	3.9	1.4	.100	1.9	0.03	11.7	19.5	0.60	0.16	40.9	8.9	-9	.480	-46	2.5	2.9
	Sound	-36.0	3.5	5.3	10	7.7	2.5	.031	2.0	0.06	9.5	15.5	0.86	0.31	29.1	11.7	6	.190	57	0.4	3.0
	Plant	-47.5	1.4	NA	NA	6.9	1.9	.030	1.6	0.52	36.0	28.4	0.71	0.49	43.3	32.1	53	-.094	170	0.3	3.2
LOS	*NIST North*	-43.7	1.0	NA	NA	1.0	0.7	.098	NA	0.00	NA	28.1	0.76	0.00	12.1	48.7	3.3	.000	18	0.0	5.4
	Child Care	-33.6	2.4	NA	NA	1.5	1.5	-.027	NA	0.00	NA	NA	0.14	0.00	6.9	20.8	0.5	.000	8	0.0	4.1
	Sound	-39.5	1.7	NA	NA	2.3	1.1	.053	NA	0.00	NA	NA	0.44	0.00	11.5	28.7	3.3	.000	25	0.0	4.2
	Plant	-47.5	1.4	NA	NA	1.5	1.6	.033	NA	0.00	NA	40.5	1.42	0.00	25.5	29.5	14.6	.000	153	0.0	3.9

B. The Reference Spatial-Temporal Response

Our model for the reference spatial-temporal response $\tilde{h}(t,\theta)$ valid at (d_0, f_c) essentially follows from (1) by augmenting $h(t)$ in the θ dimension as

$$\tilde{h}(t,\theta) = \sum_{i=1}^{N}\sum_{j=1}^{\infty}\sum_{k=1}^{\infty} \tilde{a}_{ijk} e^{j\varphi_{ijk}} \delta(t-\tau_{ijk}, \theta-\phi_{ijk}) \quad (12)$$

and exchanging a_{ijk} with $\tilde{a}_{ijk}$. In order to extract the parameters of the model, $\tilde{h}(t,\theta)$ was computed for each experiment through (5) for $f = 2$–8 GHz, however by first normalizing the measured array frequency response in (4) by the pathgain factor and so replacing it in (5) with $\tilde{h}(f,\theta) = H(f,\theta)/(d/d_0)^{-(n/2)}(f/f_c)^{-(\alpha/2)}$ instead. Note that the parameters of the pathgain model in the previous subsection were necessary to generate $\tilde{h}(t,\theta)$ and so were extracted beforehand.

Once generated, the arrival data points $(\tilde{a}_{ijk}, \varphi_{ijk}, \tau_{ijk}, \phi_{ijk})$ were extracted from the responses through the CLEAN algorithm in [16]. Only those experiments for which the distance between the transmitter and receiver exceeded 7.7 m, equivalent to the Fraunhofer distance for our UCA with $r = 24$ cm at $f_c = 5$ GHz, were used to extract $\tilde{h}(t,\theta)$ in compliance with our far-field assumption in beamforming; however in some scenarios there may have been scatterers present in the near-field of the UCA in violation of that assumption, resulting in a dilated shape of the corresponding arrival in the measured response. In order to mitigate these non-linear effects when isolating the arrivals, the power proved more robust than the complex amplitude to the discrepancies between the template spatial-temporal response used for deconvolution (see [33]) and the actual shape of each arrival which varied from path to path. The iterations of the CLEAN algorithm ceased when less than 20% residual power remained from the initial amount in the response. Only the most significant arrivals, as determined by a power threshold of 27 dB from the maximum peak in the response, were used to fit the model parameters in the sequel. Fig. 5(a) illustrates a synthetic spatial-temporal response generated from 20 arrivals by scaling the template response in amplitude and shifting it in time and angle, all three parameters distributed uniformly. The response was subsequently perturbed by substantial Gaussian noise for an equivalent $\mathrm{SNR} = -3.7$ dB.[3] At each arrival, note the distinct X sidelobe pattern of the template response.[4] Despite the low SNR, the CLEAN algorithm reliably detected all of the arrivals: the ground-truth arrivals are marked as red solid circles while the estimated arrivals are marked as black hollow circles. Fig. 5(b) shows the residual power left after all of the arrivals are identified and removed iteratively.

The reference spatial-temporal response partitions the arrivals indexed through k into N spatial clusters, or *superclusters* indexed through i, and subordinate temporal clusters, or simply *clusters* indexed through j. It reflects our measured responses composed consistently from 1) one *direct* supercluster arriving first from the direction of the transmitter and 2) one or more *wave-guided* superclusters arriving later from the door(s) (when placing the receiver in a room) or from the hallway(s) (when placing it in a hallway); the doors and hallways effectively guide the arrivals through, creating "corridors" in the response. Consider as an example the measured response in Fig. 4(a) taken in *Child Care* with three distinct superclusters highlighted in different colors. The partial floor plan in Fig. 4(b) shows the three corresponding paths colored accordingly and the coordinate (τ_i, ϕ_i) of each path appears as a dot on the response. The direct supercluster arrives first along the direct path and the later two along the wave-guided paths from the opposite directions of the hallway. We model N for NLOS through the Poisson distribution[5] as

$$N \sim \mathcal{P}(N;\eta) \quad (13)$$

and set $N = 1$ for LOS.[6]

The notion of clusters harks back to the well-known phenomenon witnessed in temporal channel modeling [1], [9], [35] caused by larger scatterers in the environment which induce a

[3]The cumulative amount of noise exceeds that of the signal as the former is spread throughout the whole response while the letter is composed from only a few arrivals.

[4]The template spatial-temporal response is formulated and illustrated in [33].

[5]$\mathcal{P}(N;\eta) = \eta^N e^{-\eta}/N!$.

[6]We actually observed two superclusters in all our LOS experiments, however the second arriving with an offset of 180° relative to the first was clearly due to the reflections off the opposite walls attributed to our testing configuration in the hallways rather than to the channel.

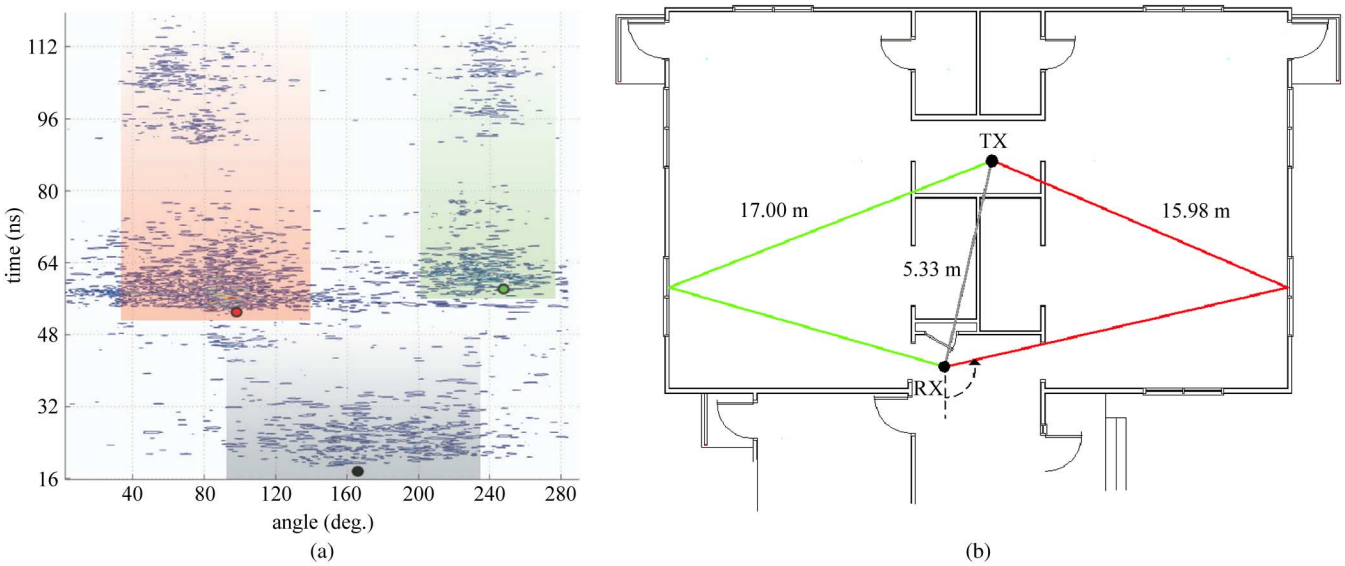

Fig. 4. A measured spatial-temporal response in *Child Care* with three distinct superclusters. (a) The response $h(t,\theta)$; (b) the partial floor plan.

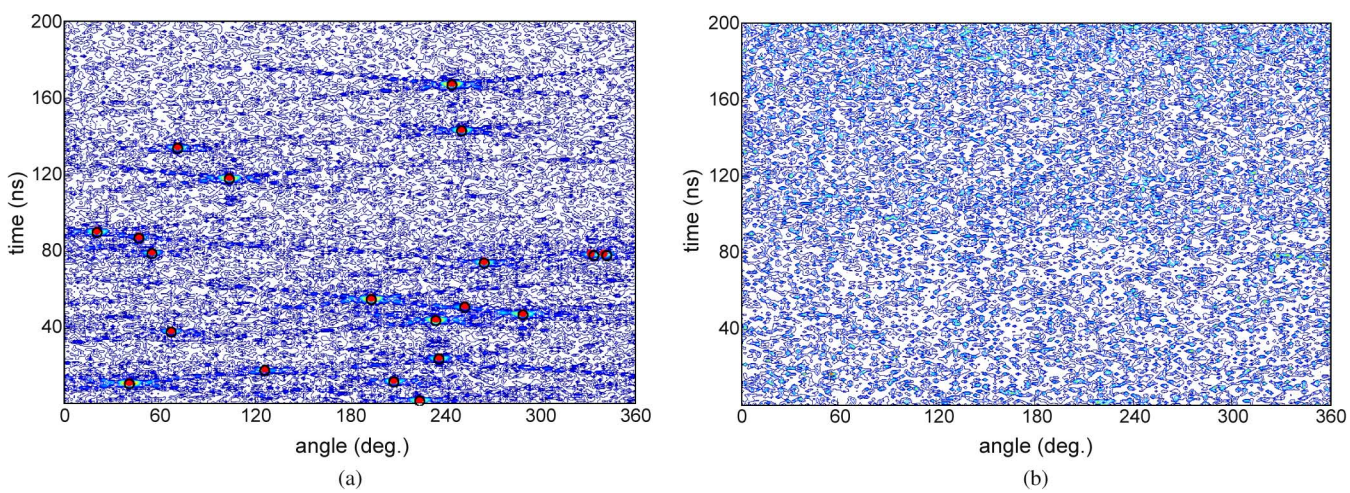

Fig. 5. A synthetic spatial-temporal response generated from 20 arrivals and perturbed by Gaussian noise. (a) Before running the CLEAN algorithm; (b) after running the CLEAN algorithm.

delay with respect to the first cluster within a supercluster. Notice the two distinct clusters of each wave-guided supercluster in Fig. 4(a).

1) The Delay τ_{ijk}: The equations in (14) govern the arrival delays. The delay τ_1 of the direct supercluster coincides with that of the first arrival. In LOS conditions, τ_1 equals the ground-truth delay $\tau_0 = d/c$, i.e. the time elapsed for the signal to travel the distance d at the speed of light c. However our previous work [33] confirms that the signal travels through walls at a speed slower than in free space, incurring an additional delay $(\tau_1 - \tau_0)$. As illustrated in Fig. 6(b), the additional delay scales with τ_0 according to Υ in (14a) since the expected number of walls in the direct path increases with ground-truth delay. Based on the well-known Saleh-Valenzuela (S-V) model [35], the delay between wave-guided superclusters $(\tau_i - \tau_{i-1})$, $i > 2$ depends on the randomly located doors or hallways and so obeys the exponential distribution[7] in (14a); so does the delay $(\tau_{ij} - \tau_{i,j-1})$ between clusters within supercluster i in (14b) and the delay $(\tau_{ijk} - \tau_{ij,k-1})$ between arrivals within cluster ij in (14c) due to randomly located larger and smaller scatterers respectively

$$\begin{aligned}
&(a)\ (\tau_1-\tau_0)=\Upsilon\cdot\tau_0, \tau_0=\frac{d}{c};\\
&\quad(\tau_i-\tau_{i-1})\sim\mathcal{E}(\tau_i-\tau_{i-1};L), i>2\\
&(b)\ (\tau_{ij}-\tau_{i,j-1})\sim\mathcal{E}(\tau_{ij}-\tau_{i,j-1};\Lambda), \tau_{n1}=\tau_n\\
&(c)\ (\tau_{ijk}-\tau_{ij,k-1})\sim\mathcal{E}(\tau_{ijk}-\tau_{ij,k-1};\lambda), \tau_{ij1}=\tau_{ij}.
\end{aligned} \tag{14}$$

2) The Angle ϕ_{ijk}: As the walls retard the delay of the direct supercluster τ_1, they also deflect its angle ϕ_1 from the ground-truth angle ϕ_0 through refraction and diffraction. Our previous work [33] reveals that the degree of deflection also scales with τ_0 according to υ in (15a). Concerning the angle of the wave-guided superclusters ϕ_i, $i > 2$, our experiments confirm the uniform distribution in (15a) supported by the notion that the

[7] $\mathcal{E}(\tau_i - \tau_{i-1}; L) = (1/L)e^{-((\tau_i-\tau_{i-1})/L)}$.

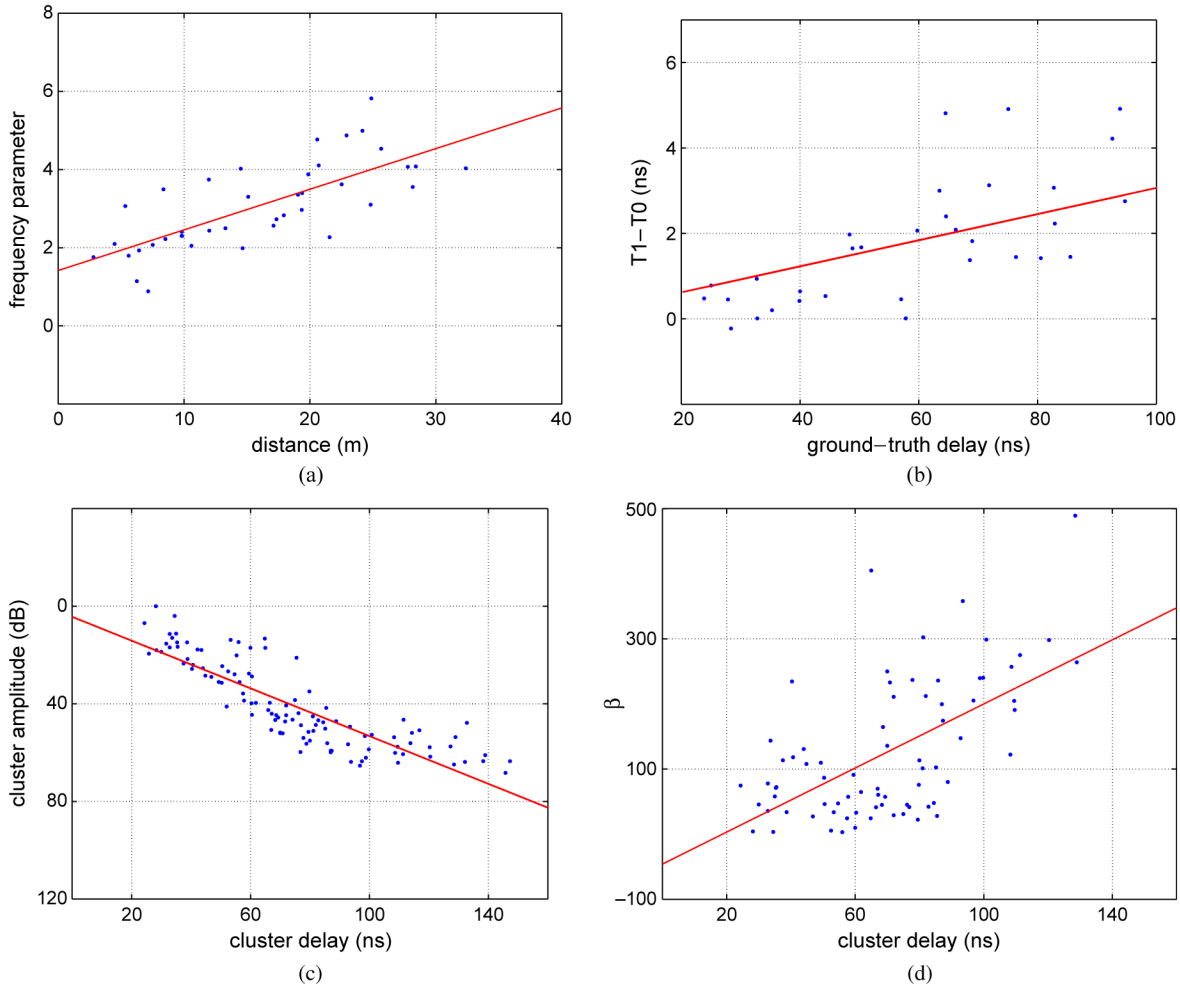

Fig. 6. Plots of selected model parameters for the *Child Care* in NLOS environment. (a) Frequency parameter versus distance; (b) $\tau_1 - \tau_0$ versus cluster delay; (c) cluster amplitude versus cluster delay; (d) β versus cluster delay.

doors and hallways could fall at any angle with respect to the orientation of the receiver. The cluster angle ϕ_{ij} in (15b) approaches from the same angle as the supercluster due to the guiding effect of the doors and hallways, and in agreement with [15]–[17] the Laplacian distribution[8] models the intra-cluster angle $(\phi_{ijk} - \phi_{ij})$, i.e. the deviation of the arrival angle from the cluster angle in (15c)

$$\begin{aligned}
&(a)\ |\phi_1 - \phi_0| = \upsilon \cdot \tau_0; \phi_i \sim \mathcal{U}(\phi_i; 0, 2\pi), i > 2\\
&(b)\ \phi_{ij} = \phi_i\\
&(c)\ (\phi_{ijk} - \phi_{ij}) \sim \mathcal{L}(\phi_{ijk} - \phi_{ij}; \sigma).
\end{aligned} \tag{15}$$

3) The Complex Reference Amplitude $\tilde{a}_{ijk}e^{j\varphi_{ijk}}$: Like in the S-V model, the cluster amplitude $\tilde{a}_{ij}$ fades exponentially versus the cluster delay τ_{ij} according to Γ in (16a) and as illustrated in Fig. 6(c); the arrival amplitude $\tilde{a}_{ijk}$ also fades exponentially versus the intra-cluster delay $(\tau_{ijk} - \tau_{ij})$ according to $\gamma(\tau_{ij})$ in (16b). Our experiments suggest a linear dependence of γ on τ_{ij} in some buildings confirmed by other researchers [1], [9]. The parameter s drawn from a Normal distribution $\mathcal{N}(s; 0, \sigma_s)$ captures the stochasticity of the amplitude, of particular use when simulating time diversity systems [5]. The arrival phase φ_{ijk} in (16c) is well-established in literature as uniformly distributed [26]

$$\begin{aligned}
&(a)\ \tilde{a}_{ij} = \tilde{a}_{11} \cdot e^{-\frac{1}{2}\frac{(\tau_{ij}-\tau_{11})}{\Gamma}}\\
&(b)\ \tilde{a}_{ijk} = \tilde{a}_{ij} \cdot e^{\frac{1}{2}\left[\frac{(\tau_{ijk}-\tau_{ij})}{\gamma(\tau_{ij})}+s\right]} \cdot e^{-\frac{1}{2}\frac{|\phi_{ijk}-\phi_{ij}|}{\beta(\tau_{ij})}}\\
&\quad \gamma(\tau_{ij}) = \gamma_0 + \gamma_1 \cdot \tau_{ij}\\
&\quad \beta(\tau_{ij}) = \beta_0 + \beta_1 \cdot \tau_{ij}\\
&\quad s \sim \mathcal{N}(s; 0, \sigma_s)\\
&(c)\ \varphi_{ijk} \sim \mathcal{U}(\varphi_{ijk}; 0, 2\pi)
\end{aligned} \tag{16}$$

We found the arrival amplitude $\tilde{a}_{ijk}$ also to fade exponentially versus the intra-cluster angle $|\phi_{ijk} - \phi_{ij}|$ according to $\beta(\tau_{ij})$ in (16b). In NLOS the walls spread the arrival amplitude in angle with each interaction on the path to the receiver. The number of expected interactions increases with the cluster delay, justifying a linear dependence of β on τ_{ij} as modeled through (16b). Fig. 6(d) illustrates this phenomenon for the *Child Care* in NLOS environment. However we exercise caution in generalizing this phenomenon as indeed it depends on the construction material: in *NIST North*, even though sheetrock walls are

[8] $\mathcal{L}(\phi_{ijk} - \phi_{ij}; \sigma) = (1/2\sigma)e^{-(|\phi_{ijk}-\phi_{ij}|/\sigma)}$.

the most favorable of the four buildings in terms of signal penetration, the aluminum studs inside the walls spaced every 40 cm act as "spatial filters", reflecting back those arrivals most deviant from the cluster angle and hence sharpening the clusters in angle with increasing cluster delay, as indicated through negative β_1; this dependence is less noticeable in *Sound* and *Plant* where we record β_1 an order of magnitude less in comparison to the other two buildings since the signal propagates poorly through cinder block and steel respectively, and so wave guidance defaults as the chief propagation mechanism. In the past, Spencer [15], Cramer [16], and Chong [17] have claimed spatial-temporal independence: for Spencer, these conclusions were drawn from experiments conducted in buildings with concrete and steel walls similar to *Sound* and *Plant* respectively, where we too notice scarce dependence; for Chong and Cramer, the dependence was less observable because the experiments were conducted at a maximum distance of 14 m.

C. Reconstructing the Spatial-Temporal Response

A stochastic spatial-temporal response can be reconstructed from our model through the following steps:

1) Select d (and in turn $\tau_0 = d/c$), ϕ_0, and the parameters from one of the eight environments in Table II;
2) Generate the stochastic variables N and ($\tilde{a}_{ijk}$, φ_{ijk}, τ_{ijk}, ϕ_{ijk}) of the arrivals from the reference spatial-temporal model in Section IV-B: set $\tilde{a}_{11} = 1$ in (16a) and then normalize the amplitudes to satisfy (9b), keeping only those clusters and arrivals with amplitude above some threshold;
3) Choose a subband in $f = 2$–8 GHz with bandwidth B and center frequency f_c, and sample interval Δf; compute $H(f)$ in (2) for each sample frequency from the pathgain model in Section IV-A and the generated arrivals;
4) Select P and compute $H_p(f)$ in (3) from $H(f)$ for each element in the circular antenna array (note that any array shape can be used by applying the appropriate steering vector);
5) Compute $H(f, \theta)$ in (4) from $H_p(f)$ which yields the sought spatial-temporal response $h(t, \theta)$ through (5).

V. Conclusions

In this paper, we have proposed a detailed spatial-temporal channel propagation model with 20 parameters for the UWB spectrum 2–8 GHz in eight different environments. The parameters were fit through an extensive measurement campaign including 160 experiments using a vector network analyzer coupled to a virtual circular antenna array. The novelty of the model captures the dependence on the signal propagation delay of the frequency parameter, the delay and angle of the first arrival, and the cluster shape. Most importantly for UWB-MIMO systems, our model discriminates between clusters arriving from the direct path along the direction of the transmitter and those guided through doors and hallways.

References

[1] A. F. Molisch, K. Balakrishnan, D. Cassioli, C.-C. Chong, S. Emami, A. Fort, J. Karedal, J. Kunisch, H. Schantz, U. Schuster, and K. Siwiak, "A comprehensive model for ultrawideband propagation channels," in *Proc. IEEE Global Commun. Conf.*, Mar. 2005, pp. 3648–3653.

[2] H. A. Khan, W. Q. Malik, D. J. Edwards, and C. J. Stevens, "Ultra wideband multiple-input multiple-output radar," in *Proc. IEEE Radar Conf.*, May 2005, pp. 900–904.

[3] W. P. Siriwongpairat, W. Su, M. Olfat, and K. J. R. Liu, "Multiband-OFDM MIMO coding framework for UWB communications systems," *IEEE Trans. Signal Processing*, vol. 54, no. 1, Jan. 2006.

[4] L. Yang and G. B. Giannakis, "Analog space-time coding for multi-antenna ultra-wideband transmissions," *IEEE Trans. Commun.*, vol. 52, no. 3, March 2004.

[5] A. Sibille, "Time-domain diversity in ultra-wideband MIMO communications," *EURASIP J. Appl. Signal Processing*, vol. 3, pp. 316–327, 2005.

[6] Z. Irahhauten, H. Nikookar, and G. J. M. Janssen, "An overview of ultra wide band indoor channel measurements and modeling," *IEEE Microw. Wireless Compon. Lett.*, vol. 14, no. 8, Aug. 2004.

[7] S. S. Ghassemzadeh, L. J. Greenstein, T. Sveinsson, A. Kavcic, and V. Tarokh, "UWB delay profile models for residential and commercial indoor environments," *IEEE Trans. Veh. Technol.*, vol. 54, no. 4, Jul. 2005.

[8] D. Cassioli, A. Durantini, and W. Ciccognani, "The role of path loss on the selection of the operating band of UWB systems," in *Proc. IEEE Conf. on Personal, Indoor and Mobile Commun.*, Jun. 2004, pp. 3414–3418.

[9] D. Cassioli, M. Z. Win, and A. F. Molisch, "The ultra-wide bandwidth indoor channel: From statistical model to simulations," *IEEE J. Sel. Areas Commun.*, vol. 20, no. 6, Aug. 2002.

[10] S. M. Yano, "Investigating the ultra-wideband indoor wireless channel," in *Proc. IEEE Conf. on Veh. Technol., Spring*, May 2002, pp. 1200–1204.

[11] C. Prettie, D. Cheung, L. Rusch, and M. Ho, "Spatial correlation of UWB signals in a home environment," in *Proc. IEEE Conf. on Ultra Wideband Systems and Technologies*, May 2002, pp. 65–69.

[12] A. Durantini, W. Ciccognani, and D. Cassioli, "UWB propagation measurements by PN-sequence channel sounding," in *Proc. IEEE Conf. on Commun.*, Jun. 2004, pp. 3414–3418.

[13] A. Durantini and D. Cassioli, "A multi-wall path loss model for indoor UWB propagation," in *Proc. IEEE Conf. on Veh. Technol., Spring*, May 2005, pp. 30–34.

[14] J. Kunisch and J. Pump, "Measurement results and modeling aspects for the UWB radio channel," in *Proc. IEEE Conf. on Ultra Wideband Systems and Technologies*, May 2002, pp. 19–24.

[15] Q. H. Spencer, B. D. Jeffs, M. A. Jensen, and A. L. Swindlehurst, "Modeling the statistical time and angle of arrival characteristics of an indoor multipath channel," *IEEE J. Sel. Areas Commun.*, vol. 18, no. 3, Mar. 2000.

[16] R. J.-M. Cramer, R. A. Scholtz, and M. Z. Win, "Evaluation of an ultra-wide-band propagation channel," *IEEE Trans. Antennas Propag.*, vol. 50, no. 5, May 2002.

[17] C.-C. Chong, C.-M. Tan, D. I. Laurenson, S. McLaughlin, M. A. Beach, and A. R. Nix, "A new statistical wideband spatio-temporal channel model for 5-Ghz band WLAN systems," *IEEE J. Sel. Areas Commun.*, vol. 21, no. 2, Feb. 2003.

[18] K. Haneda, J.-I. Takada, and T. Kobayashi, "Cluster properties investigated from a series of ultrawideband double directional propagation measurements in home environments," *IEEE Trans. Antennas Propag.*, vol. 54, no. 12, Dec. 2006.

[19] N. Czink, X. Yin, H. Ozcelik, M. Herdin, E. Bonek, and B. H. Fleury, "Cluster characteristics in a MIMO indoor propagation environment," *IEEE Trans. Wireless Commun.*, vol. 6, no. 4, April 2007.

[20] J. Medbo and J.-E. Berg, "Spatio-temporal channel characteristics at 5 GHz in a typical office environment," in *IEEE Veh. Technol. Conf., Fall*, pp. 1256–1260.

[21] K. Yu, Q. Li, D. Cheung, and C. Prettie, "On the tap and cluster angular spreads of indoor WLAN channels," in *Proc. IEEE Veh. Technol. Conf., Spring*, pp. 218–222.

[22] A. S. Y. Poon and M. Ho, "Indoor multiple-antenna channel characterization from 2 to 8 GHz," presented at the IEEE Conf. on Commun., May 2003.

[23] S. Venkatesh, V. Bharadwaj, and R. M. Buehrer, "A new spatial model for impulse-based ultra-wideband channels," presented at the IEEE Veh. Technol. Conf., Fall, Sep. 2005.

[24] W. Zhang, T. D. Abhayapala, and J. Zhang, "UWB spatial-frequency channel characterization," presented at the IEEE Veh. Technol. Conf., Spring, May 2006.

[25] H. Hashemi, "The indoor radio propagation channel," *Proc. IEEE*, vol. 81, no. 7, pp. 943–968.

[26] X. Li and K. Pahlavan, "Super-resolution TOA estimation with diversity for indoor geolocation," *IEEE Trans. Wireless Commun.*, vol. 3, no. 1, Jan. 2004.
[27] C. A. Balanis, *Antenna Theory: Analysis and Design, Second Edition*. New York: Wiley, 1997.
[28] T. B. Vu, "Side-lobe control in circular ring array," *IEEE Trans. Antennas Propag.*, vol. 41, no. 8, Aug. 1993.
[29] S. Zwierzchowski and P. Jazayeri, "A systems and network analysis approach to antenna design for UWB communications," in *IEEE Antennas Propag. Society Symp.*, Jun. 2003, pp. 826–829.
[30] J. Keignart and N. Daniele, "Subnanosecond UWB channel sounding in frequency and temporal domain," in *Proc. IEEE Conf. on Ultra Wideband Systems and Technologies*, May 2002, pp. 25–30.
[31] R. Vaughan and J. B. Andersen, "Channels, propagation and antennas for mobile communications," *IET Electromagnetic Wave Series 50*, 2003, Appendix A.
[32] C. Gentile and A. Kik, "A frequency-dependence model for the ultrawideband channel based on propagation events," *IEEE Trans. Antennas Propag.*, vol. 56, no. 2, pp. 2775–2780, Aug. 2008.
[33] C. Gentile, A. J. Braga, and A. Kik, "A comprehensive evaluation of joint range and angle estimation in ultra-wideband location systems for indoors," *EURASIP J. Wireless Commun. Netw.*, 2007, id. 86031.
[34] C. Gentile and A. Kik, "A comprehensive evaluation of indoor ranging using ultra-wideband technology," *EURASIP J. Wireless Commun. Netw.*, 2008, id. 248509.
[35] A. Saleh and R. A. Valenzuela, "A statistical model for indoor mulipath propagation," *IEEE J. Sel. Areas Commun.*, vol. 5, pp. 128–137, Feb. 1987.

Camillo Gentile received the B.S. and M.S. degrees from Drexel University, Philadelphia, PA, and the Ph.D. degree from the Pennsylvania State University, University Park, all in electrical engineering.

He has been a Researcher in the Advanced Network Technologies Division, National Institute of Standards and Technology (NIST), Gaithersburg, MD, since 2001. His current interests include RF location systems, channel modeling, and smart grids. He served as the Technical Editor for the location annex of the IEEE 802.15.4a standard. In the past, he has worked in the areas of computer vision, pattern recognition, and neural networks.

Sofía Martínez López received the Telecommunications Engineer degree from the Universidad Politécnica de Cartagena, Spain and the Ph.D. degree from the Ecole Nationale Supérieure des Télécommunications, France.

She is currently working for the Orange-France Télécom Group, where she is involved in quality supervision and optimization of the 3G mobile network. Her areas of research interests include radio channel parameter estimation and wireless communication systems.

Alfred Kik was born in Rayak, Lebanon, on November 30, 1978. He received the Electrical Engineering degree from the Lebanese University, in 2001, and a Specialized Masters degree from the Ecole Nationale Supérieure des Télécommunications, Paris, France, in 2004.

From 2005 to 2007, he was with the National Institute of Standards and Technology, Gaithersburg, MD, as a Guest Researcher. He was involved in evaluating localization techniques for emergency applications and in UWB indoor channel modeling. Since 2008, he is with the Tokyo Institute of Technology, Tokyo, Japan, working toward the Ph.D. degree. His main research interests are electromagnetic compatibility and materials metrology.

Mr. Kik is a member of The Institute of Electronics, Information and Communication Engineers (IEICE), Japan.